



**HAL**  
open science

## Topological search of the crack pattern from a continuum mechanical computation

Marina Bottoni, Frédéric Dufour, Cédric Giry

### ► To cite this version:

Marina Bottoni, Frédéric Dufour, Cédric Giry. Topological search of the crack pattern from a continuum mechanical computation. *Engineering Structures*, 2015, 99, pp.346-359. 10.1016/j.engstruct.2015.05.005 . hal-01545335

**HAL Id: hal-01545335**

**<https://hal.science/hal-01545335>**

Submitted on 15 Mar 2022

**HAL** is a multi-disciplinary open access archive for the deposit and dissemination of scientific research documents, whether they are published or not. The documents may come from teaching and research institutions in France or abroad, or from public or private research centers.

L'archive ouverte pluridisciplinaire **HAL**, est destinée au dépôt et à la diffusion de documents scientifiques de niveau recherche, publiés ou non, émanant des établissements d'enseignement et de recherche français ou étrangers, des laboratoires publics ou privés.



Distributed under a Creative Commons Attribution - NonCommercial 4.0 International License

# Topological search of the crack pattern from a continuum mechanical computation

Marina Bottoni<sup>a,b,\*</sup>, Frédéric Dufour<sup>c</sup>, Cédric Giry<sup>d</sup>

<sup>a</sup>EDF R&D/AMA, 828 Boulevard des Maréchaux, F-91762 Palaiseau Cedex, France

<sup>b</sup>IMSIA/Université Paris Saclay, UMR 9219 EDF-CNRS-CEA-ENSTA, 828 Boulevard des Maréchaux, F-91762 Palaiseau Cedex, France

<sup>c</sup>3SR/Université Grenoble Alpes, UMR 5521, Domaine universitaire, BP 53, F-38041 Grenoble Cedex 9, France

<sup>d</sup>LMT-Cachan/ENS-Cachan/CNRS/Université Paris Saclay, UMR 8535, 61 avenue du Président Wilson, F-94230 Cachan, France

In this contribution, a method to track the crack path from a continuum finite element simulation using failure material models is presented. The work belongs to a larger project, aiming at extracting the crack opening a posteriori of a continuum finite element computation to deal with durability assessment of concrete structures. Cracking is modelled in a diffuse manner by a distribution of an appropriate scalar state variable associated to material degradation. With the proposed method, the crack path is found in the post-processing phase by means of a step-by-step procedure. At each step, a new location point is computed where the state variable is maximum in a given direction at a given distance. Furthermore a specific procedure is proposed to detect multiple cracks in an automatic way. The proposed method is successfully applied to two studies implying either a single crack or a multi-crack pattern, obtained with different continuum models to highlight the versatility of the proposed approach.

## 1. Introduction

A correct evaluation of crack path and opening is important in many concrete engineering applications.

For some type of structures, crack opening estimation is required in relation with permeability issues, in order to limit fluid releases. Examples are confinement vessels and cooling towers of nuclear power plants, dams and liquid natural gas reservoirs [41,16,38]. In any case, since concrete is exposed to environmental agents, the knowledge of crack characteristics may be exploited in order to assess durability, in the sense of penetration of external chemical aggressive agents [5] or simply for aesthetic reasons. Finally, even design codes prescribe as a service limit state a maximum crack opening which in turn must be addressed carefully.

The assessment of the mechanical state of structures is more and more often obtained by numerical simulations, the finite element method being by far the most employed technique. The mechanical simulation of a degraded or fractured structure can be performed at present days following different approaches.

A first approach, based on fracture mechanics, assumes the existence of a crack or a set of potential cracks. The crack is then

modelled as a discontinuity, sometimes by describing it explicitly in the geometry [19], sometimes by enriching with Heaviside functions the interpolation of displacements in the element, as in the X-FEM method [28,30,29]. Due to the direct incorporation of the discontinuity, this approach is here referred to as *discrete*. Using such a method has the clear advantage, that crack properties (crack path and opening) are retrieved directly, because they are main variables of the model. It is also true that X-FEM has allowed to overcome some traditional shortcomings of discrete approaches, such as necessity of incremental remeshing [3] or constraints on crack path direction for cohesive elements, which otherwise must be known a priori [19]. However, this approach has still a limitation when it comes to describe appropriately the dissipative bulk behaviour (i.e. microcracking and kinematic field across the fracture process zone) on one hand, and crack initiation on the other hand.

A completely different approach, called here *continuum approach*, consists in adopting a nonlinear constitutive law, where the degradation state of the material is described by at least one state variable [2,21,22]. Through continuum models the description of both crack initiation and propagation in the same frame is possible. A further benefit of the continuum with respect to discrete approach lies in the correct description of the degradation process for quasi-brittle materials, from diffuse damage to formation of the macro-crack due to coalescence of micro-cracks. In other terms, in quasi-brittle materials energy dissipation takes

\* Corresponding author at: EDF R&D/AMA, 828 Boulevard des Maréchaux, F-91762 Palaiseau Cedex, France.

E-mail address: marina.bottoni@edf.fr (M. Bottoni).

place in a volume of non negligible size with respect to the characteristic size of the structure; this volume is usually called Fracture Process Zone (FPZ). Unfortunately, continuum approaches do not directly provide the crack path and opening.

A third alternative, more and more explored by researchers, consists in adopting both approaches at the same time. An embedded or explicitly meshed discontinuity models the macro-crack, while a non-linear constitutive law is used to model the diffuse damage [1,32]. However, intrinsic difficulties may arise by establishing the transition point between the two kind of approaches whatever the mechanical quantity used for the equivalence [8,42]. Some recent works provide arguments to overcome this problem by proposing a transition between a damage model and a cohesive zone approach [7,24], but still there are limitations on the crack direction. Finally, the method of thick level sets [31] seems very promising in the next future.

The choice made in this contribution is to perform a continuum nonlinear computation based on classical finite element method and then retrieve the crack characteristics a posteriori in a post-processing phase. The complete procedure is two fold; in a first step the crack path is estimated and in the second step the crack opening along the found crack path is computed. For the latter phase, it is possible to establish a strain equivalence with a strong discontinuity [11]; another method consists in computing a displacement jump by isolating the inelastic part if any of the strain tensor concurring to open the crack, so ignoring the elastic part released upon unloading [26]. In order to obtain the crack path, a method has recently been developed in [10], inspired by the Global Tracking Method used in [33,32]; the crack path is an isoline of a scalar field obtained from a secondary gradient problem. However, this method is, so far, limited to radial loading and mode I failure, since it is based on the assumption that, at the time the crack path is computed, the principal direction of the largest principal strain is perpendicular to the crack. Furthermore, this is not verified at the intersection between a FPZ and a rebar in concrete. The aim of this new contribution is thus to obtain the crack path in an automatic way for a wider range of mechanical problems.

In the first part of this paper, the method for tracking the crack path is presented. In a second stage, choices of numerical parameters are discussed. Thirdly, two continuum models used for illustrative purposes are briefly described. Finally, the powerfulness of the method is analysed on two testcases.

## 2. Description of the algorithm

### 2.1. General discussion

The key idea is to search a crack path as a ridge in the topological three-dimensional space generated by the scalar field  $X(x, y)$ , i.e. a state variable field representing material degradation from a 2D simulation. This state variable can be an internal variable of a continuum model, such as isotropic damage or one component of an anisotropic damage model [9]; it can also be a plastic deformation or the hardening/softening variable, when plasticity models are used; eventually, it can also be an effective strain or a strain component, since strain localizations take place when modelling a crack by means of a continuum model. Since several variables are possible for a given continuum model, the best choice is the one with the sharpest edges on the ridge sides. Besides, in order to reduce the search domain to cracked zones and to split apart those zones in case of multiple cracks, the identification of one ore more portions of domain is possible by imposing a lower limit  $X_0$  to the field, so that points in each region will respect the condition:  $|X| > X_0$ . Each area is referred here as the numerical Fracture Process Zone (FPZ) and is associated to one single crack.

In the defined space, the ridge can be defined as the line in the  $xy$  plane connecting two points on which the average field value is maximum. However, a direct application of this definition is not straightforward. In fact, the starting and ending points of the ridge are not known a priori. For example, there is no knowledge of crack tip, usually assumed as the starting point in incremental propagation, due to the post-processing character of the proposed method.

Another property of the defined 3D-space is that the intersection between it and a plane (or a more general surface) yields to a curve, having its maximum on the crack path. In the proposed algorithm, this feature is exploited in a step-by-step procedure, in which a new point belonging to the crack path is found at each step.

Actions performed in each step are described in Section 2.2. In the initiation step (see Section 2.3), the procedure is slightly different than the one executed in the typical step since the starting point and the search direction are not known. Criteria for stopping the procedure once the complete crack path is found are given in Section 2.4. The topological search is accomplished on one FPZ at a time. In Section 2.5, the method for searching in a domain with multiple cracks is described. As a result of the algorithm, one obtains a series of points belonging to the crack path. So, a first approximation of the crack path can be obtained by connecting successive pairs of points with a segment. Higher order approximations, i.e. higher order interpolating polynomials, could eventually be used to ensure for instance  $C^1$  continuity if needed.

### 2.2. Running step

Actions performed in the typical step need a *starting point* and a *search direction*. At step  $i$ , the starting point is the point  $P_{i-1}$  belonging to the crack path and found in the previous step  $i-1$ ; the search direction  $\overrightarrow{P_{i-2}P_{i-1}}$  is determined by the two previous points on the crack path. With reference to the diagram in Fig. 1, the following detailed operations are carried out at the current step  $i$ .

- (1) A *prediction point*  $P_i^{pr}$  is defined by moving from the starting point in the search direction, at a distance  $a$  called *search length*.
- (2) The field  $X(x, y)$  is projected onto a line of length  $l_{orth}$ , perpendicular to the search direction and passing through  $P_i^{pr}$ ; the one-variable function  $X(s)$  is obtained, being  $s$  the abscissa along this line. In the finite element frame, the projection is performed on discrete points.

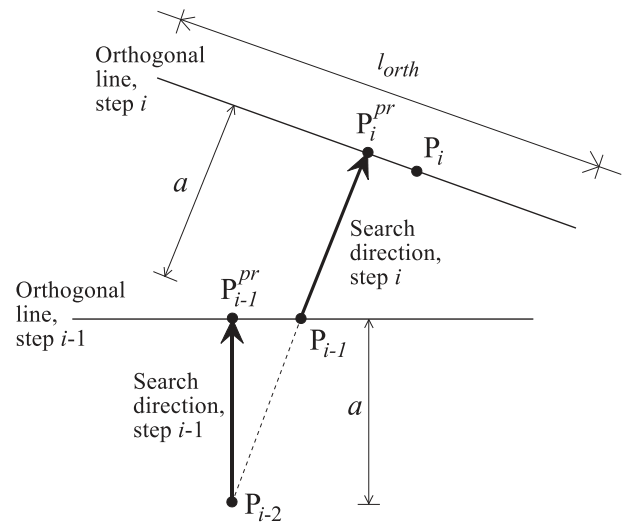


Fig. 1. Scheme of the topological search procedure.

- (3) The new crack path point  $P_i$  is the one where the function  $X(s)$  is maximum.

Due to spatial discretization or to practical implementation of field projection in finite element codes, field  $X(x,y)$  and consequently its projection  $X(s)$  are mostly not  $C^1$  continuous. The irregularity of the profile  $X(s)$  affects usually that of the crack path. Hence, it may be convenient to smooth the function  $X(s)$  to loosen dependency on the mesh topology. Many smoothing methods do exist in literature; the moving average or the Polynomial Approximation with Exponential Kernel (PAEK) method are two examples. A smoothing length  $l_{smth}$  is required by most methods. In this contribution, the smoothing of function  $X(s)$  is realized by a convolution product by means of a Gaussian function  $\phi(\|\zeta - s\|)$ :

$$\bar{X}(s) = \int_{l_{orth}} \phi(\|\zeta - s\|) X(\zeta) d\zeta \quad (1)$$

with:

$$\phi(\|\zeta - s\|) = \exp \left[ -\frac{(\|\zeta - s\|)^2}{2l_{smth}^2} \right] \quad (2)$$

The choice of the smoothing length is a compromise between a too small value that will not smooth enough the profile although it preserves all details and a too large value that accounts for values out of the computational domain. Analysis on the optimal value in the case of the convolution product with Gaussian function is provided at Section 3.4.

The convolution integral of Eq. (1) must be evaluated numerically. To do so, the main variable  $s$ , i.e. the curvilinear abscissa, must be sampled. Let  $\delta_{orth}$  be the sample step, so that there are  $n = l_{orth}/\delta_{orth}$  intervals on  $l_{orth}$ . By supposing the function value constant on the general interval of length  $\delta_{orth}$ , the integral of Eq. (1) can be approximated by the following expression:

$$\bar{X}(n \cdot \delta_{orth}) \approx \sum_{i=1}^{N_{orth}} \delta_{orth} \cdot X(i\delta_{orth}) \cdot \phi(\|n\delta_{orth} - i\delta_{orth}\|) \quad (3)$$

From the numerical point of view, the field  $\bar{X}(s)$  is stored on  $N_{orth}$  points. Hence, the point distance  $\delta_{orth}$  has to be seen as the lateral precision of the crack path.

### 2.3. First step

In order to apply the operations described in Section 2.2, at least the first two points  $P_1$  and  $P_2$  of the crack path must be known. Once their location is determined, two possible search directions are then defined:  $\overrightarrow{P_1P_2}$  and  $\overrightarrow{P_2P_1}$ . The search continues

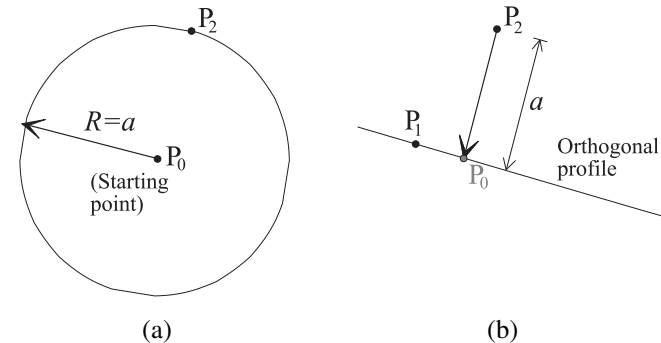


Fig. 2. Initialisation of the topological search: (a) determination of the second point  $P_2$ , (b) back-correction of the first point  $P_0$  to  $P_1$ .

independently in both identified directions as detailed in Section 2.2 until stop requirements are fulfilled (see Section 2.4).

The aim of the first step, considered as the procedure initiation, is the determination of  $P_1$  and  $P_2$ . The first step differs slightly from the characteristic step in some details. With reference to the diagram in Fig. 2, the following operations are performed:

- (1) An approximation  $P_0$  of the first point  $P_1$  is found and corresponds to the absolute maximum value of the field  $X(x,y)$  on the considered FPZ.
- (2) The field  $X(x,y)$  is projected onto the circle, with  $P_0$  as the centre, so to obtain the field  $X(s)$  (see Fig. 2(a)). The radius of the circle should be about twice the finite element size and not much smaller, in order to capture local variations of the field correctly.
- (3) The projected field  $X(s)$  is smoothed by applying the line integral of Eq. (1) along the circle.
- (4) The second point  $P_2$  of the crack path locates where the smoothed field  $\bar{X}(s)$  is maximum (see Fig. 2(a)); unlike  $P_0$ ,  $P_2$  is obtained from the smoothed field, so it belongs to the crack path.
- (5) A backward correction is made on  $P_0$  to find an improved position for the first point  $P_1$ . As shown in Fig. 2(b) the field is projected and smoothed on the line passing through  $P_0$  and orthogonal to  $\overrightarrow{P_2P_0}$ . This correction is necessary because without the smoothing, the first point position would be too strongly dependent on the mesh, as already pointed out in Section 2.2.

### 2.4. Criteria to stop the search in one direction

The first situation for stopping the topological search in one direction is when the crack path reaches one of the domain boundaries. In practice, the procedure is stopped when the prediction point is located outside the domain.

The second situation occurs when the field value of the newly found point of the crack path is smaller than a prescribed threshold  $X_{lim}$ . Beyond this threshold, the computed crack opening is considered to have no meaning.

### 2.5. Extension to 3D and multiple cracks

So far, the presentation of the procedure is for 2D mechanical computations only and for a single FPZ.

Application to 3D cases is straightforward, if the topological search is performed on cross-sections of the three-dimensional domain. The crack surface is then reconstructed from the crack lines in each cross-section with a discretization step equal to the distance between two cross-sections.

The case of multiple cracks is a little more complicated, so it requires detailed explanations. Some steps are in fact added to the procedure described in Sections 2.2 and 2.3, in order to automatically detect every crack paths. The described method is valid within the hypothesis of distinct cracks (i.e. cracks do not cross), as a unique FPZ is associated exclusively to one crack. This hypothesis is most of the time verified for monotonic loading.

In the following list, the steps of the method are detailed, eventually modified with respect to the procedure described in Sections 2.3 and 2.2.

- (1) *Beginning of the search on the whole domain  $\Omega$ .* The procedure is initialised as detailed in Section 2.3, thus on the crack to which the absolute maximum of the field on the whole domain  $\Omega$  belongs to.

(2) *Detection of the crack path and of FPZ boundaries.* FPZ boundaries can be detected on the function  $\bar{X}(s)$  at the same time of the search of the maximum. The location of the point  $P_i$  corresponds to the closest maximum to the prediction point  $P_i^{pr}$ . In the case of close cracks, the orthogonal line may have a second peak which corresponds to another FPZ, as shown for example in Fig. 3.

Thus, this step of the procedure allows to select the right maximum along the 1D profile. Then, the two minima  $P_i^l, P_i^r$  closest to  $P_i$  are located. The space between these two minima defines the limits of the FPZ on the orthogonal line (see again Fig. 3).

At this point of the discussion, one must keep in mind that the choice of the  $l_{smth}$  should not affect too much the location of maximum and minimum values. Clearly, this length must be smaller than the crack spacing.

- (3) *Definition of the FPZ.* After the search of the single crack is ended, the FPZ boundary is known by a cloud of points. For a good identification of the FPZ area, a polynomial regression is performed to find its contour  $\mathcal{C}$ . For our applications a fourth-order polynomial has been found to be accurate enough.
- (4) *Reset of the field.* The area obtained at the previous step and defined by its boundary  $\mathcal{C}$  is the FPZ associated to the already found crack. Inside, the field is reset to a value corresponding to no damage, i.e. the crack is somehow erased. The underlying hypothesis, is that the non-linearities occurring inside this area are considered to participate exclusively in the opening of the crack associated to this area.
- (5) *Search of the next crack.* The search of the next crack begins with the new absolute maximum of the resetted field. This way, the eliminated FPZ cannot affect the new search.

Now that the procedure extension to 3D and multiple crack pattern is shown to only rely on practical issues, the parametric study is performed on 2D conditions.

### 3. Discussion on parameters range

Overall, the procedure is based on the use of five numerical parameters: the search length  $a$ , the smoothing length  $l_{smth}$ , the orthogonal line length  $l_{orth}$ , the point density on the orthogonal line  $\delta_{orth}$  and the value  $X_{lim}$  to arrest the search on the single FPZ.

Due to spatial discretization, the field  $X(x, y)$  is usually known only on a set of points on the considered domain  $\Omega$ . Depending on the finite element solution, the field  $X$  has seldom an interpolation of order higher than linear. In this section for the sake of clarity, parameter calibration is based on the assumption of a piecewise linear interpolation of the discretized field  $X(x, y)$ . After projection on a line, function  $X(s)$  is also piecewise linear. The symbol  $\Delta$  indicates the average length of the segment where  $X(s)$  is linear. The nodes defining this segment correspond to the intersections of the orthogonal line with the finite element edges.

#### 3.1. Length of the orthogonal line

The length of the orthogonal line does not affect the result of the algorithm, provided that:

- it is longer than the FPZ width, so that the function  $X(s)$  is correctly represented;
- it is long enough such that the smoothing function  $\phi(s)$  used in the convolution product is not too much truncated around  $s$ . In such a way, the influence of  $\phi(s)$  to build the smoothed function  $\bar{X}(s)$  is well taken into account. For the Gaussian function,

truncation at a distance of  $2l_{smth}$  is acceptable, being  $\phi(2l_{smth}) \approx 0.13$  since only the location of the extrema is looked for, not their actual value.

By calling  $D$  half of the FPZ width, one can then assume:  $l_{orth} = 2(D + 2l_{smth})$ . This length is obtained by adding  $2l_{smth}$  on both sides of the FPZ. This value for  $l_{orth}$  has been used throughout the following testcases.

#### 3.2. Point density on the orthogonal line

As mentioned in Section 2.2 the point density  $\delta_{orth}$  is the lateral precision of the crack path. In order to loosen mesh dependency, a density of at least  $\Delta/10$  is then necessary.

#### 3.3. Limit value for the crack search

Limit value  $X_{lim}$  does not affect the accuracy of the search, so it will not be discussed in detail. Obviously, the choice depend on the physical meaning of the state variable  $X$  in the continuum model. An hint on how to fix this parameter in the case of damage models has been provided in [11], where a method to associate an error to the computed crack opening at each point of the crack path is suggested. Actually, strictly speaking the crack is completely created only when damage has reached the value of 1, i.e. complete failure, on the orthogonal profile. However, one can think that the crack is almost formed also for values smaller than 1. In other words, for damage models  $X_{lim}$  is related to the transition from diffuse damage to a real crack.

Other arguments for fixing the  $X_{lim}$  value should be related to the purpose of the crack opening computation. One can cite, for example, Pijaudier-Cabot et al. [37] who suggested a law for dealing the transition in transfer properties from diffuse damage and a well-formed crack. In this perspective,  $X_{lim}$  is chosen to give a correct estimation of leakage.

As discussed,  $X_{lim}$  cannot be uniquely defined. It depends on the choice of the state variable and on the problem solved after the crack path is found.

#### 3.4. Smoothing length

The effect of the smoothing length has been tested on piecewise linear functions  $X(s)$ . The  $X(s)$  functions employed to test parameters are generated numerically in order to dispose of an unlimited number of profiles. To do so, a parametric exponential function is sampled on the nodes of a line, distance between each node being equal to  $\Delta$ . The function values range in the interval  $[0; 1]$ ; the adopted orthogonal length is  $20\Delta$ , with the fracture process zone ( $X > 0$ ) of size  $2D = 14$ . Then, a corrective random term is added to nodal values, in order to make the profile non-symmetrical. Actually, real  $X(s)$  functions are almost never symmetrical since:

- the domain is discretized through an unstructured mesh;
- the domain is discretized through a structured mesh, but the crack path does not intersect elements on their edges.

An uniform random distribution of range  $[-0.1; 0.1]$  is used to perturb the profile symmetry. This interval, controlling the magnitude of the additional term, is calibrated on real profiles, and looking at several continuum models and meshes. That guarantees a high level of dissymmetry, typical of coarse meshes. An example of obtained  $X(s)$  function is given by the blue<sup>1</sup> line in Fig. 4, where

<sup>1</sup> For interpretation of colour in Figs. 4 and 14, the reader is referred to the web version of this article.

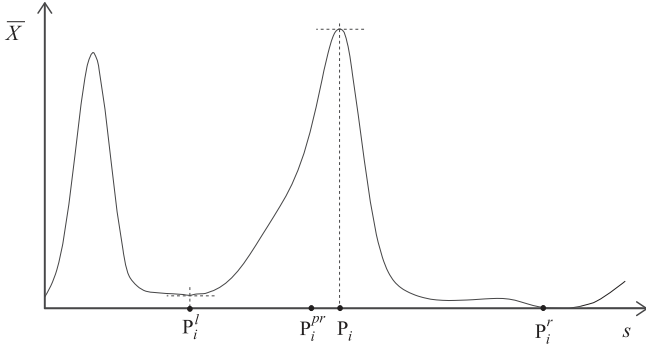


Fig. 3. Search of points belonging to the crack path and to FPZ boundaries.

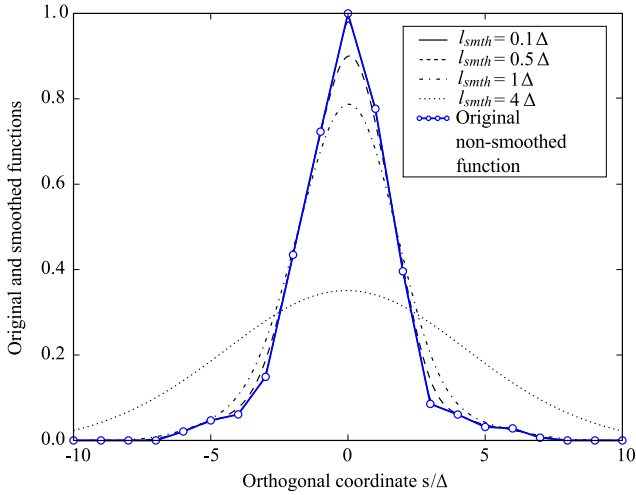


Fig. 4. Original  $X(s)$  and smoothed  $\bar{X}(s)$  profiles with different smoothing lengths.

the normalized abscissa  $s/\Delta$  is used. In the same figure, four smoothed functions  $\bar{X}(s)$  are also depicted. They are obtained by adopting a point density  $\delta_{orth} = 0.001\Delta$  on the orthogonal line. For a smoothing length of  $0.1\Delta$ , the original (non-smoothed) and smoothed profiles are almost superposed, so that  $l_{smth}$  should at least be larger than  $0.5\Delta$  to have a minimum smoothing effect. Obviously, a unique value of  $l_{smth}$  giving the *real* crack position does not exist, since this parameter has only a numerical role. Nevertheless, it is suggested to use a small value while retaining adequate smoothing

properties, so to avoid a too severe flattening of the profile or merging of two close FPZs. The parameter can then be taken in the range  $[0.5\Delta; 2\Delta]$ .

Under the hypothesis of a piecewise linear function, the maximum on the orthogonal line of the non-smoothed function is always on a node. As already mentioned, this could result in a strong mesh-dependency of the crack path. The effect of the smoothing length must then be studied with respect to the position of the maximum of the smoothed profile, corresponding to the point belonging to the crack path. To this purpose, different  $X(s)$  profiles and smoothing lengths are tested, observing the position of the crack path point. With the assumed random effect, the variation in the position is never bigger than  $D/10$ , which is acceptable.

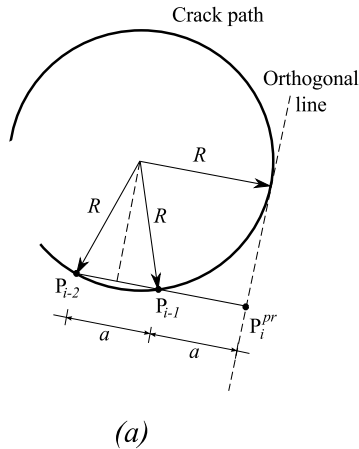
### 3.5. Search length

The choice of the minimum search length depends essentially on the crack path curvature, as shown here by testing the algorithm on the portion of a circle with radius  $R$ .

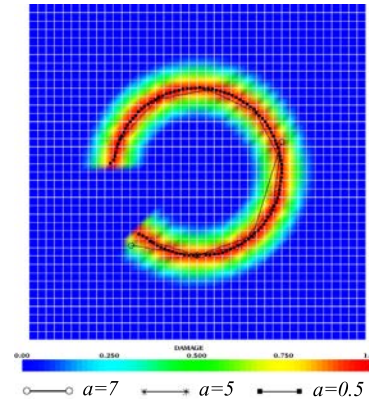
This property can be proven easily with the help of simple geometric considerations, as shown in Fig. 5(a). Indeed, the represented configuration is a limit case, where the orthogonal line does not cross the crack path, since it is tangent to it. The corresponding relationship between  $a$  and  $R$  is  $R = 3/2a$ , so that the maximum value of the ratio  $a/R \approx 0.67$  is proposed. Adoption of a smaller search length assure that points obtained by the algorithm lay on the crack path.

In order to confirm this property, a test is performed by applying the method onto a heuristic numerical 2D-field for different values of the search length. This field is completely defined by a given crack path, equal to a portion of a circle having radius  $R$ , a given FPZ width equal to  $2D$ , and a given shape on a line orthogonal to the crack path. In our example,  $R = 10$ ,  $2D = 5$  and on the orthogonal line the field have a parabolic shape, with values in the range  $[0; 1]$ . A squared specimen of size  $40 \times 40$  is considered. Finally, the field is discretized on a regular squared mesh of element size  $\Delta = 1$ . The search algorithm is applied with following parameters other than the search length: the orthogonal and smoothing lengths are  $l_{orth} = 20$  and  $l_{smth} = 1$ ; the point density on the orthogonal line is  $\delta_{orth} = 0.004$ ; the limit value for stopping the search is  $X_{lim} = 0.4$ .

In Fig. 5, the obtained crack paths for three search lengths are provided:  $a = 0.5$ ,  $a = 5$ ,  $a = 7$ , corresponding to ratios  $a/R$  equal  $0.05$ ,  $0.5$  and  $0.7$  respectively. The test shows that with a ratio  $a/R = 0.5$ , the crack path is retrieved but not really accurate. The



(a)



(b)

Fig. 5. Crack path on a numerical field for different search lengths.

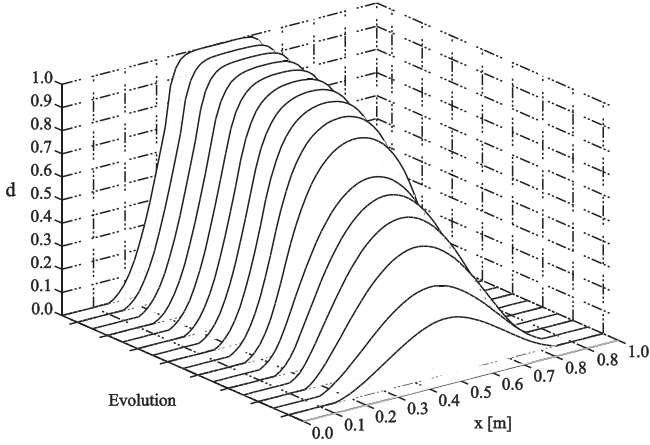


Fig. 6. Mazars' damage model: numerical 1D profiles for damage.

algorithm fails for  $a/R = 0.7$  which is larger than the limit value of 0.67. As for small  $a$  values, there seems to be no lower limit: for  $a = 0.05\Delta$  the right crack path is still obtained.

Other tests have been performed by modifying the field characteristics or the mesh refinement, so adopting a different curvature, the FPZ width, an exponential shape on the orthogonal line, or a finer mesh. Conclusions on the ratio  $a/R$  remain identical.

The value  $a/R = 0.67$  is the limit ratio to obtain points belonging to the crack path. However, in the perspective of leakage computations, accuracy should be determined with regard to the purpose of calculating the crack opening, the precision on the direction of the crack normal being directly related to the definiteness of the crack path. It is then recommended to run the algorithm several times with decreasing search lengths and to check for convergence. For the computation of the flow rate the reader is addressed for example to [11,39,17]. Moreover, thanks to the low computational cost of the crack search algorithm, there are no drawbacks to use small search steps, in order to obtain a path as smooth as possible.

#### 4. Continuum models used in the examples

In this section, the continuum models employed for the illustrative applications are summarized. Two isotropic damage models have been used to highlight the versatility of the proposed method. Both are associated to two different regularisation techniques, since conventional continuum damage descriptions suffer from ill-posedness beyond a certain level of damage and lead to spurious localizations. A certain number of regularisation techniques exist in literature, such as the integral [36,15], the strain gradient [35] or the damage gradient [12] approaches. Regularized damage models are often called *non-local*, since the damage evolution depends on the mechanical state in a neighbourhood of the material point.

In a first example, a brittle isotropic damage model is used; the regularization of the solution is obtained by enriching the formulation with the damage gradient [25]. In a second example, the Mazars' damage model [27] is employed in association with a non-local integral regularization.

The relationship between the stress and the strain tensors has the following form:

$$\boldsymbol{\sigma} = A(d)\mathbf{E} : \boldsymbol{\varepsilon} \quad (4)$$

being  $\mathbf{E}$  the elastic stiffness tensor,  $\boldsymbol{\sigma}$  the Cauchy stress tensor and  $\boldsymbol{\varepsilon}$  the small strain tensor, and with  $A$  a stiffness function varying from 0 to 1. As already mentioned, the nonlocal quantities appear in the damage evolution equation, as well as in the yield function  $f$ ; since

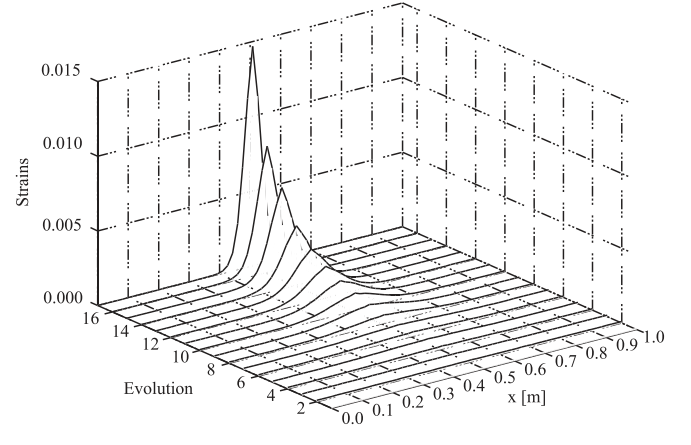


Fig. 7. Mazars' damage model: numerical 1D profiles for equivalent strain.

the exact expression of both depends on the constitutive law, they are given separately for the two models. Finally, the Kuhn-Tucker consistency conditions take the simple form, with the dot denoting time differentiation:

$$f(\boldsymbol{\varepsilon}) \leq 0; \quad \dot{d} \geq 0; \quad \dot{d}f(\boldsymbol{\varepsilon}) = 0 \quad (5)$$

##### 4.1. A brittle gradient damage model

This law has been developed in the frame of the generalized standard materials (see [14] or [18]), extended to a gradient constitutive law, as shown in [23,25].

Constitutive equations are still given by Eq. (4) while the damage driving force reads:

$$Y = -\frac{1}{2}A'(d)\boldsymbol{\varepsilon} : \mathbf{E} : \boldsymbol{\varepsilon} \quad (6)$$

where  $A(d)$  is the stiffness function. The yield criterion is:

$$f(Y, \nabla^2 d) = Y + c\nabla^2 d - k \quad (7)$$

which is completed by the Kuhn-Tucker conditions, Eq. (5). In Eq. (7),  $k$  is a yield threshold; the control of damage localization is modelled through the introduction of the Laplacian of damage  $\nabla^2 d$ , being  $c > 0$  a parameter governing the coupling between neighbouring material points, hence the strength of the nonlocal effects. Additional boundary and interface conditions are required due to

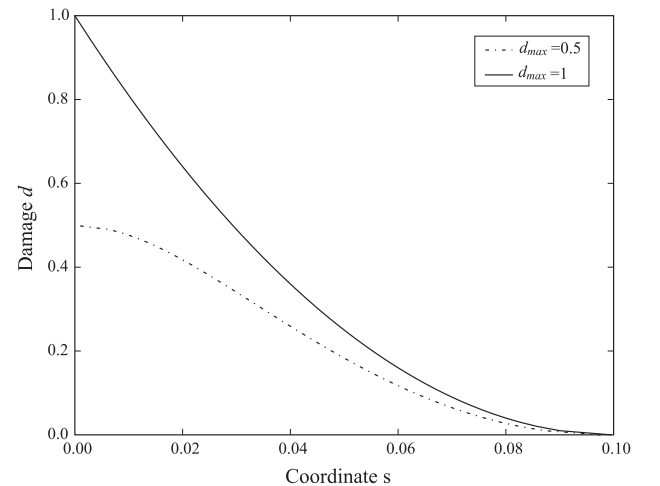


Fig. 8. Brittle gradient damage model: analytical 1D profiles for damage.

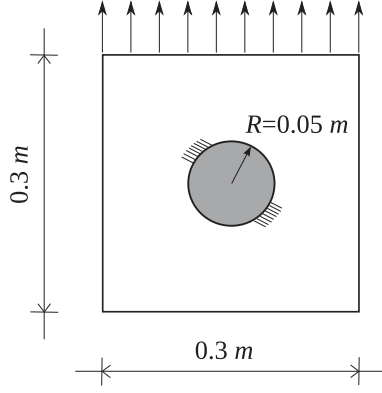


Fig. 9. Geometry and boundary conditions of the specimen with circular inclusion.

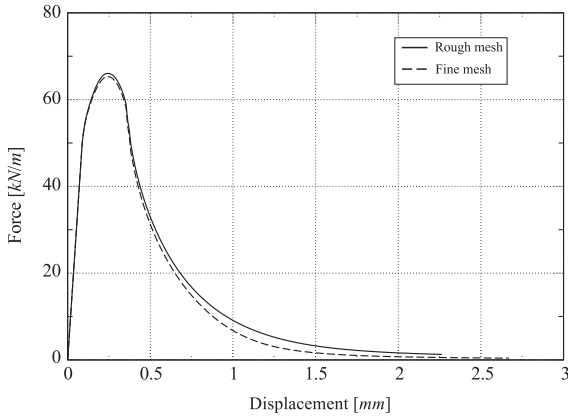


Fig. 10. Specimen with circular inclusion: force-displacement plot with mesh refinement.

the differential formulation of the model. By denoting  $\partial\Omega$  the boundary of the body domain  $\Omega$ ,  $\mathbf{n}$  its outer normal,  $\Gamma$  a potential surface of discontinuity,  $\mathbf{v}$  its normal and  $[[\bullet]]$  the discontinuity of a quantity across  $\Gamma$ , they read:

$$[[d]] = 0 \quad \text{and} \quad [[c \nabla d]] \cdot \mathbf{v} = 0 \quad \text{across } \Gamma \quad (8)$$

$$\nabla d \cdot \mathbf{n} = 0 \quad \text{on } \partial\Omega \quad (9)$$

The corresponding Helmholtz free energy and dissipation potential at the structural level are respectively:

$$\mathcal{F}(\boldsymbol{\varepsilon}, d) = \int_{\Omega} \left( \frac{1}{2} A(d) \boldsymbol{\varepsilon} : \mathbf{E} : \boldsymbol{\varepsilon} + \frac{c}{2} \nabla d \cdot \nabla d \right) dV \quad (10)$$

$$\mathcal{D}(\dot{d}) = \int_{\Omega} \left( k \dot{d} + \mathcal{I}_{\mathbb{R}^+}(\dot{d}) \right) dV \quad (11)$$

with  $\mathcal{I}_{\mathbb{R}^+}$  the indicator function which enforces  $\dot{d} \geq 0$ .

The stiffness function  $A(d)$  depends on the additional parameter  $\gamma$ :

$$A(d) = \left( \frac{1-d}{1+\gamma d} \right)^2 \quad (12)$$

Besides the elastic parameters  $E$ ,  $\nu$ , the brittle law is finally described by three parameters  $k$ ,  $c$  and  $\gamma$ . It can be shown that for a 1D problem, they can be related to three macroscopic parameters (see [24]), that is the peak stress  $\sigma_y$ , the fracture energy  $G_f$  and half the localization band at failure  $D$  through equations:

$$k = \frac{3G_f}{4D}, \quad c = \frac{3}{8}DG_f, \quad \gamma = \frac{3EG_f}{4\sigma_y^2 D} - 1 \quad (13)$$

#### 4.2. Nonlocal Mazars' damage model

The yield criterion for the Mazars' damage model is expressed in terms of strains and reads:

$$f = \bar{\varepsilon}_{eq} - H \quad (14)$$

where  $\bar{\varepsilon}_{eq}$  is a nonlocal equivalent strain and  $H$  is a history variable, a function strictly growing upon loading with  $\varepsilon_{d0}$  as initial value, i.e. the damage threshold. The nonlocal effective strain is found by application of the nonlocal equation to the local variable  $\varepsilon_{eq}$ , defined as:

$$\varepsilon_{eq} = \sqrt{\sum_{i=1}^3 \langle \varepsilon_i \rangle_+^2} \quad (15)$$

where  $\langle \bullet \rangle_+$  denotes the positive part of a quantity. The nonlocal equivalent of  $\varepsilon_{eq}$  at point  $\mathbf{x}$  is obtained by averaging it on the domain  $\Omega$  with a weighting function  $\Psi$ , in the following way:

$$\bar{\varepsilon}_{eq}(\mathbf{x}) = \frac{\int_{\Omega} \Psi(\|\boldsymbol{\xi} - \mathbf{x}\|) \varepsilon_{eq}(\boldsymbol{\xi}) dV}{\int_{\Omega} \Psi(\|\boldsymbol{\xi} - \mathbf{x}\|) dV} \quad (16)$$

A Gaussian function  $\Psi$  is used as a possible weighting function:

$$\Psi(\|\boldsymbol{\xi} - \mathbf{x}\|) = \exp\left(-\left(\frac{2\|\boldsymbol{\xi} - \mathbf{x}\|}{l_c}\right)^2\right) \quad (17)$$

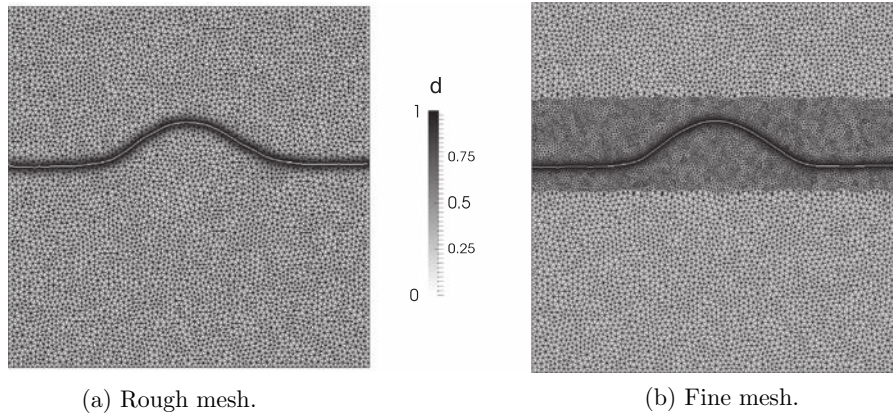


Fig. 11. Specimen with circular inclusion: meshes and damage maps.

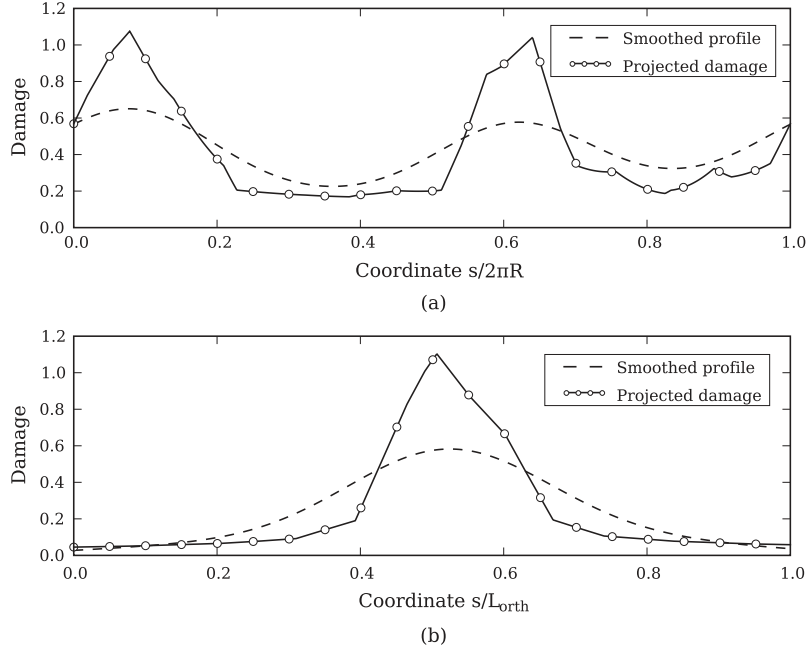


Fig. 12. Specimen with circular inclusion: projected and smoothed damage (a) on the circle during initialisation procedure, (b) on one orthogonal profile.

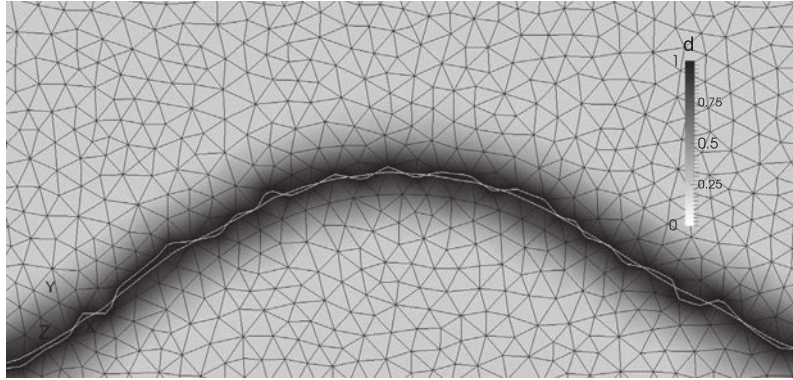


Fig. 13. Specimen with circular inclusion: crack paths for a smoothed or a non smoothed orthogonal profile.

where  $\|\xi - \mathbf{x}\|$  is the distance to the considered point  $\mathbf{x}$  and  $l_c$  is the internal length of the non-local damage model. The evolution law for damage is a function of the history variable  $H$ :

$$d_c = 1 - \frac{\varepsilon_{d0}(1 - A_c)}{H} - A_c \exp(-B_c(H - \varepsilon_{d0})) \quad (18)$$

$$d_t = 1 - \frac{\varepsilon_{d0}}{H} \exp(-B_t(H - \varepsilon_{d0})) \quad (19)$$

where  $t$  is for tension and  $c$  for compression; also,  $B_t$ ,  $A_c$ ,  $B_c$  are law parameters as well as the damage threshold  $\varepsilon_{d0}$ . Actually, Eq. (19) does not correspond to the original expression, but to that proposed by [20] to improve behaviour in tension. The final value for the damage  $d$  is obtained by averaging damages in tension and compression with the coefficient  $\alpha_t$ :

$$d = \alpha_t d_t + (1 - \alpha_t) d_c \quad (20)$$

In Eq. (20),  $\alpha_t$  is given by:

$$\alpha_t = \frac{\sum_{i=1}^3 \langle \varepsilon_i \rangle_+ \varepsilon_{ti}}{\varepsilon_{eq}^2}; \quad \varepsilon_t = \frac{1 + \nu}{E} \langle \sigma \rangle_+ - \frac{\nu}{E} \text{tr}(\langle \sigma \rangle_+) \quad (21)$$

where  $\nu$  and  $E$  are the Poisson's ratio and the Young's modulus respectively.

The stiffness function of Eq. (4) simply reads:

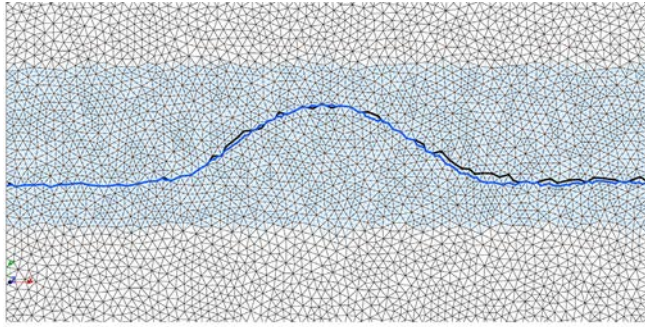
$$A(d) = 1 - d \quad (22)$$

#### 4.3. Fields used in the crack path search

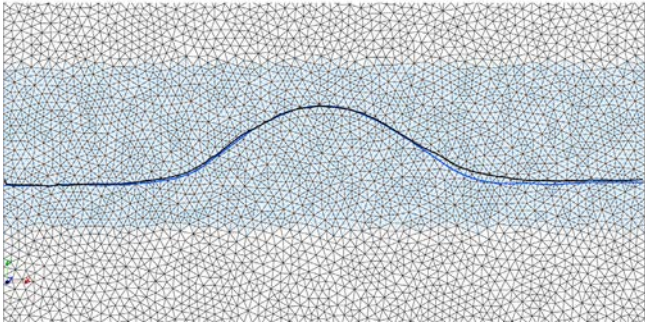
An important point concerns the choice of the field used for the crack path search. From what has been described in previous sections, the algorithm is meaningful as long as a unique maximum on the orthogonal profile can be clearly defined.

An indication of the shape of damage on the orthogonal profile can be obtained in an unidimensional problem. This allows us to compare the two models introduced in the previous sections.

Concerning the Mazars' model, a bar is loaded by applying an increasing axial displacement to one end and constraining it to the other end. The unidimensional problem is obtained by using 121 2D isoparametric elements together with a zero value of the Poisson ratio. The bar is 1 m long, damage model parameters are  $\varepsilon_0 = 10^{-4}$ ,  $B_t = 1000$ ,  $l_c = 0.18$  m (parameters  $A_c$  and  $B_c$  are not involved under these boundary conditions), the Young modulus is equal to 33,700 MPa. In order to initiate damage, a central element is weakened by adopting a Young modulus equal to 31,000 MPa.



(a) Non smoothed orthogonal profile.



(b) Smoothed orthogonal profile.

**Fig. 14.** Comparison of crack paths with mesh refinement.

After solving numerically the problem through the finite element solver *Cast3M*, one obtains the damage profiles of Fig. 6; here, the internal variable  $d$  is depicted as a function of position  $x$  along the bar and for different loading levels. It is quite clear that, while damage is approaching 1, it spreads out around the point of maximum and the saturated region covers an increasing length in the middle of the bar (and not only at the point representing the

crack). This is a well-known drawback for strain-based regularization techniques, due to a mutual coupling between damage and strain localization. In fact, on the one hand strains (and so the equivalent strain governing damage) are increased by the presence of damage reducing stiffness. On the other hand, arising of damage on a sound point can be provoked by non-locality; through Eq. (16) local strains are in fact averaged with high strains of the neighbouring damaged points. A detailed investigation of this damage diffusion effect for strain-gradient regularizations is provided in [13], while the close relationship between nonlocal integral models, employed in the present paper, and strain gradient models is given for example in [34]. It is then quite clear that a damage field obtained using the nonlocal Mazars' model cannot be directly employed for crack path search. However, history variable has properties similar to damage, since it accounts for loading history but without any upper limit. Indeed, in an uniaxial monotonic test, the history variable is very close to the equivalent strain; this one is given in Fig. 7. Due to its shape, it is possible to use the history variable field in place of damage for our purposes; the second application presented in this paper is an example.

As mentioned in the introduction, recent research on damage models concerns an improved representation of material degradation near failure. To this frame belongs a recent proposal for a modification of the nonlocal integral regularization, with the internal length  $l_c$  depending on the stress state ([15]). Another way of improvement is given by the damage gradient approach described in Section 4.1. For this model, the damage profile can be obtained analytically in the case of uniaxial loading if the bar length is large enough so that the boundary conditions do not interfere with damage development and in the case of a prescribed displacement at both ends of the bar; this last hypothesis allows assuming a symmetrical solution for the localization band. This solution is a function of the material parameters except the elastic properties and of the maximum value of damage  $d_{max}$  reached on the bar [25]. In Fig. 8, the damage profile is given for two values of  $d_{max}$  and obtained for parameters  $G_f = 100 \text{ N/m}$ ,  $D = 0.1 \text{ m}$  and  $\sigma_y = 3 \text{ MPa}$ . The solution in terms of damage is depicted between  $x = 0$  (the centre of the bar) and the length  $D$ , since for  $x > D$  there

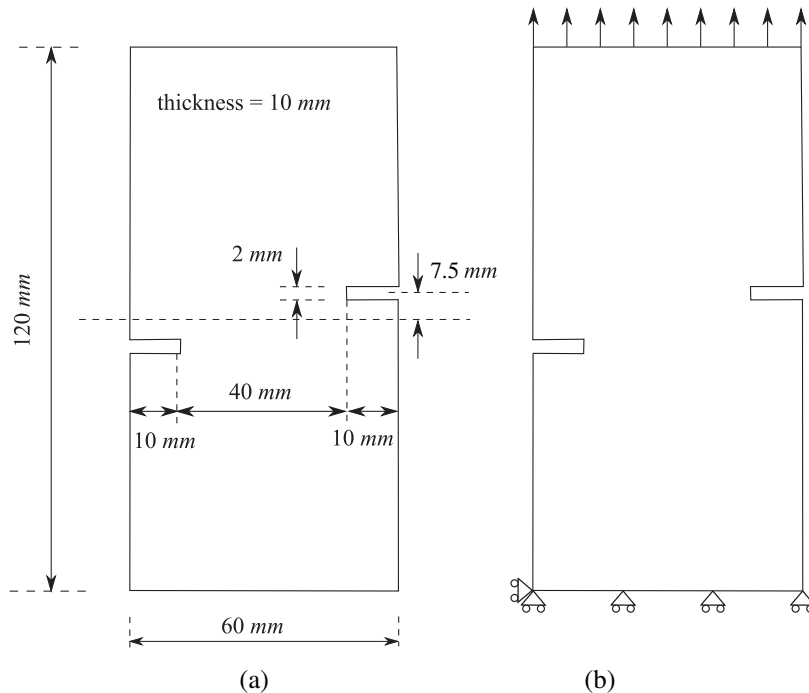


**Fig. 15.** Double-notched specimen: (a) geometry, (b) boundary conditions.

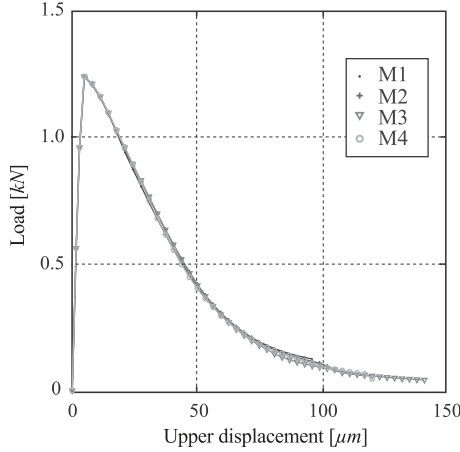


Fig. 16. Double-notched specimen, global behaviour.

is no damage. One can observe that the damage profile possesses from the beginning a well-defined maximum and that it becomes even sharper at failure ( $d = 1$ ). For this reason, the crack path search can be performed directly on the damage field.

## 5. Examples

### 5.1. Specimen with fixed circular inclusion

A first example is a squared specimen with a fixed circular inclusion. The specimen is 0.3 m by 0.3 m, the inclusion has a radius equal to 0.05 m and is located in the middle of the specimen. An imposed displacement is applied on the upper horizontal edge, while displacements of the inclusion are set to zero in all directions (see Fig. 9). The finite element code *Code\_Aster* [4] is used. The specimen is computed up to its complete failure by means of the brittle damage model of Section 4.1. Law parameters are:  $E = 30,000$  MPa,  $G_f = 100$  N/m,  $\nu = 0.2$ ,  $D = 0.01$  m,  $\sigma_y = 3$  MPa. The lower part of the specimen (starting from its geometrical centre) is considered as linear elastic, with Young modulus and Poisson

ratio equal to those of the upper part. The numerical implementation of the damage model is realized on elements with quadratic interpolations for displacements; damage is modelled as an additional degree of freedom, but adopting a linear interpolation on the finite element. The resulting field is then step-wise linear and  $C^0$  continuous on nodes.

The damage computation is performed on two meshes. Element size for the rough mesh is about 5 mm, so that four elements are included in the process zone. The fine mesh is obtained refining locally the zone of the rough mesh where the crack is expected; the original elements are split up in four new triangles, so that the local resulting size is about 2.5 mm. This way, the possible solutions of the discrete problem on the rough mesh form a subset of those on the finer mesh. The results obtained for the two meshes are tested in order to compare the behaviour of the damage model with refinement and the corresponding crack paths.

Damage maps together with their meshes are shown in Fig. 11(a) and (b). The force-displacement graph is plotted in Fig. 10, showing that computations have almost, but not completely, converged with mesh refinement.

The topological search is performed on the damage field, so that  $X = d$ . Crack paths are computed using  $l_{smth} = 5$  mm and so equal to the element size of the rough mesh as well as two times the size of the fine mesh. The adopted search step is very fine in order to underline the smoothness of the final path. The orthogonal length is 0.1 m; threshold value for stopping the procedure is fixed to 0, but the procedure stops at the time the crack path runs out the domain. The resulting crack path is also shown in Fig. 11(a) and (b).

In Fig. 12 the projected and smoothed damage profiles during the search are represented. In Fig. 12(a), the initialisation phase is shown, i.e. damage as a function of the normalized curvilinear abscissa on the circle. Since the circle intersects twice the FPZ, there are two local maxima; the procedure selects the largest one for practical purposes, but the choice of the other maximum is completely equivalent, since once the procedure has reached the domain boundary, it starts again in the other direction from the initiation point. In Fig. 12(b), damage as a function of the orthogonal normalized abscissa is depicted for one current step.

A zoom to the crack path for the rough mesh is shown in Fig. 13. Both crack paths obtained with and without smoothing the

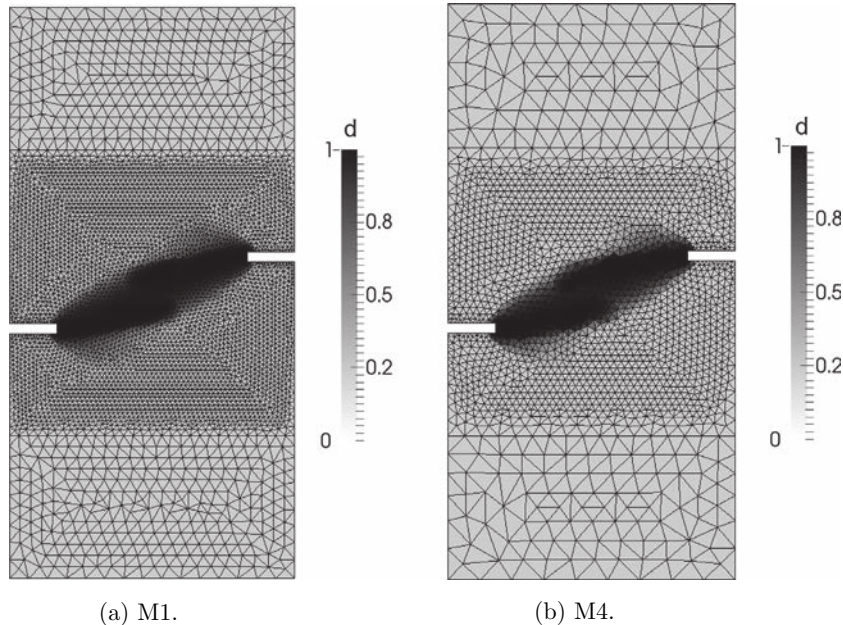


Fig. 17. Damage fields for the finest (M1) and roughest (M4) meshes.

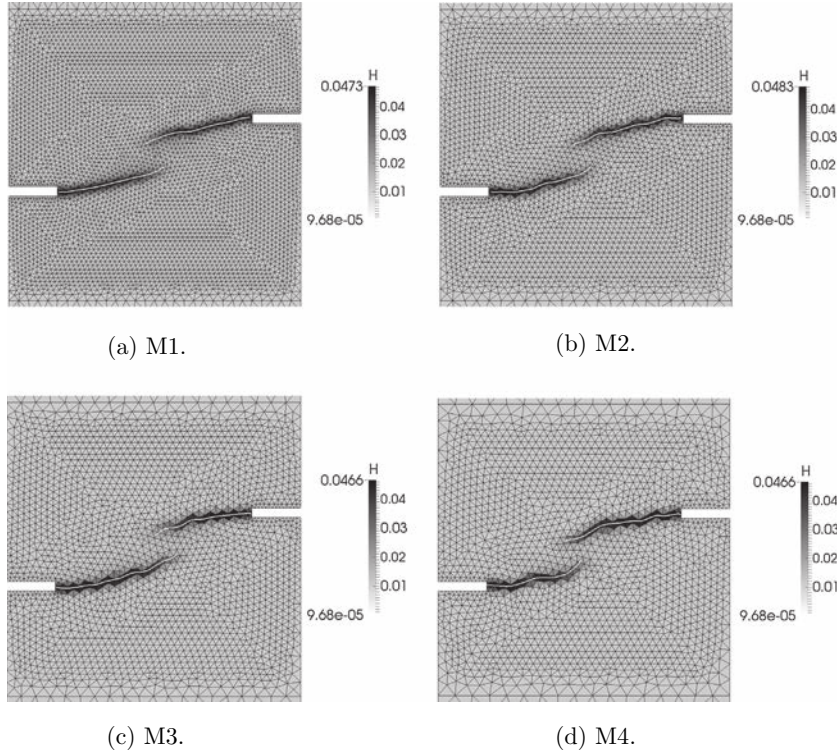


Fig. 18. History variable field and crack paths for four mesh refinements: zoom in the central part of the specimen.

orthogonal damage profile are compared. In the first case, smoothing yields a regular crack path; in the second case, the crack path coincides with element sides, as expected, so showing the importance of smoothing.

Concerning convergence with mesh refinement, nonlocal damage models are often tested on the global more than on the local behaviour. A typical approach consists in plotting a force–displacement graph which is meaningful for the studied specimen and that for meshes increasingly refined (as done in Fig. 10 for the present example). This procedure is certainly adequate in an unidimensional test, but it may be incomplete for more complex geometries or boundary conditions, where the crack path is not trivial. Actually, it may happen that close solutions are found corresponding to slightly different spatial discretizations, since the space where solutions are searched for (defined by mesh topology and adopted interpolation functions) is not exactly the same. Hence, slightly different solutions can be found during the refinement

process and that can only be observed by comparing the crack paths. This again prove the importance of applying a crack search algorithm.

In the presented case of specimen under traction with fixed inclusion, the crack paths obtained with our algorithm but without smoothing are shown in Fig. 14(a) and correspond to the paths really provided by the discrete model. The rough mesh is drawn in black and is superposed to the fine one, drawn in blue. The two crack paths are depicted with the same colour code and thicker lines. It can be observed that crack paths are close but not superposed. This difference is partly due to the fact that the finer mesh describe better the mechanical problem. However, on the right part of the specimen the distance between the two paths is bigger than the rough element size, meaning that a slightly different solution was found. In Fig. 14(b) are given the crack paths obtained by smoothing. It can be noted that the paths are superposed or very close when also the unsmoothed crack paths coincide or when their distance is equal to the fine element size. When two different solutions are found without smoothing, obviously the smoothed crack paths are also not close. Comparing paths obtained with and without smoothing, it is interesting to notice that regularity of the field and of the crack path are strongly correlated, as announced in Section 2.2.

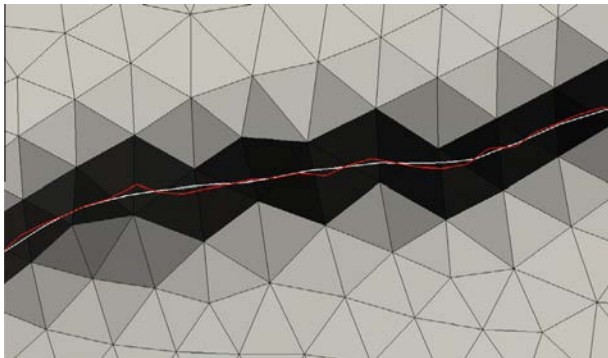
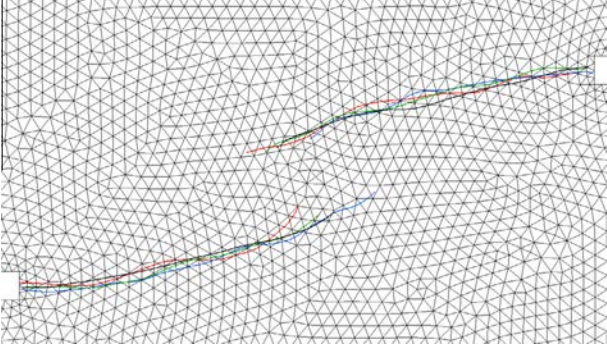


Fig. 19. Comparisons between crack paths with (white line) or without (red line) nodal averaging, for roughest mesh M4. (For interpretation of the references to colour in this figure legend, the reader is referred to the web version of this article.)

## 5.2. Double-notched specimen in tension

In this section, the procedure is applied to the F.E. results of a double-notched specimen in tension, whose geometry and boundary conditions are shown in Fig. 15. The specimen is loaded with a prescribed increasing displacement at one extremity up to failure. The corresponding experimental tests are described in details in [40]. Results given here have been obtained with the nonlocal Mazars' model described in Section 4.2, with parameters: Young modulus,  $E = 31,000$  MPa, Poisson ratio,  $\nu = 0.2$ , damage threshold,  $\varepsilon_{d0} = 0.000097$ ,  $B_t = 100$ ,  $A_c = 1.25$ ,  $B_c = 1000$ ; the internal



**Fig. 20.** Double-notched specimen, crack paths for all meshes: M1 (black), M2 (green), M3 (blue), M4 (red). (For interpretation of the references to colour in this figure legend, the reader is referred to the web version of this article.)

length of the nonlocal model is  $l_c = 0.02$  m. The finite element code *Cast3M* [6] has been used for the computation and the post-processing.

The finite element formulation of the given model is based on a linear isoparametric element; triangular elements are used. The same simulation has been run on four meshes with growing refinements. In the central part of the specimen, where damage actually is located, tested meshes have element size equal to 1 mm, 1.3 mm, 1.6 mm, 1.9 mm and are named M1, M2, M3, M4, respectively. The adopted element size, smaller than the characteristic length of 10 times for the roughest mesh, should guarantee

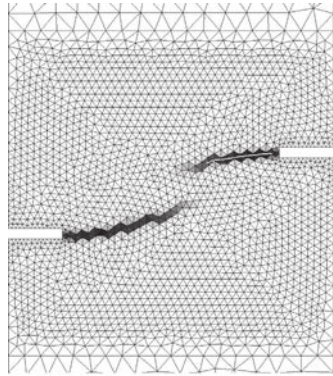
convergence of the computation, usually attained for this kind of model with about 5–6 elements in the damaged zone.

In order to compare the behaviour for different meshes, results are first examined in terms of resultant force against applied upper displacement (see Fig. 16). The plot shows that, at the global level, convergence is reached, as expected, since corresponding curves are superposed.

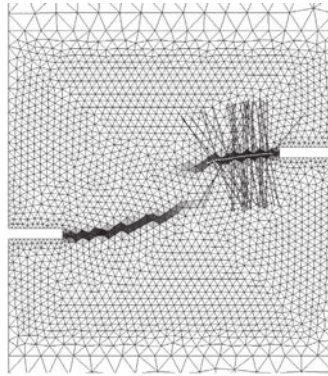
The distribution of damage on the specimen at the end of the computation is shown in Fig. 17 for meshes M1 and M4. At the end of the computation, a single damaged zone is observable in the middle of the specimen. Nevertheless, progress of the computation shows two distinct cracks developing from the notches, with the two damaged zones gradually merging. These two cracks are still recognizable from two distinct zones in the history variable map, as displayed in Fig. 18 for all four meshes.

The topological search is applied to the history variable field  $H$ , as discussed in Section 4.3. The search algorithm exploits the method described in Section 2.5 to move from one crack to the other. Retrieved crack paths are superposed to the history variable map in Fig. 18. For the search algorithm, following parameters are used:  $l_{smth}$  equal to the element size,  $a = 0.5$  mm,  $l_{orth} = 50$  mm,  $\delta_{orth} = 0.01$  mm; the algorithm is stopped for a field value equal to 15% of the maximum value, in order to limit the search to those areas where the crack is well defined.

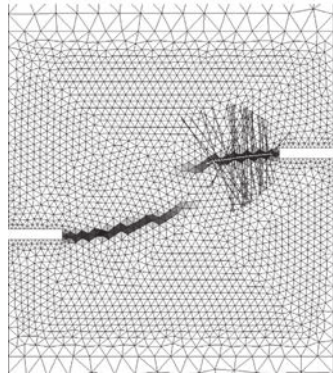
It has been stated before that field smoothing is done with the specific purpose to make the crack path mesh independent. It has been observed in the previous example that, strictly speaking, this is only possible when the same solution of the discrete problem is found, hence, when the damage model has converged at the global



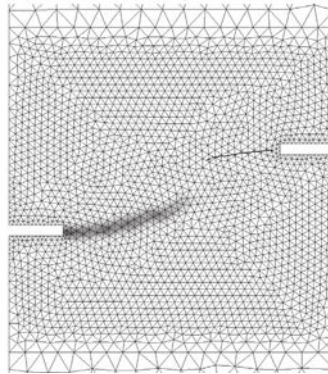
(a) Location of the first crack.



(b) Identification of the FPZ limit points on each 1D profiles.



(c) Cutting of the profiles at the FPZ boundary.



(d) Reset of the history variable field inside the FPZ.

**Fig. 21.** Double-notched specimen: steps of the multiple crack search.

and local level. So, a minimum precision is needed in the finite element description of the field to provide the converged crack path.

As is well known, the accuracy of the finite element model depend on both mesh refinement and the interpolation degree of the fields involved. Concerning the numerical implementation of the Mazars' model in the code *Cast3M*, damage and the history variable are not degrees of freedom of the finite element model. Indeed, they are recorded as state variables at the unique Gauss point of each element, so that field continuity is not assured between elements and the discrete field can be considered step-wise constant. In order to conform to the hypotheses adopted to find the optimal parameters range in Section 3, a  $C^0$ -continuous field has been retrieved by averaging on each node of the mesh the field values of each element holding the considered node. This operation leads obviously to an information loss with respect to the original field but increases its regularity. Then, the search algorithm has been applied on both the original discontinuous field and on the  $C^0$ -continuous field; crack paths of Fig. 18 refer to this second case. The numerical procedure has been able to retrieve slightly more regular crack paths on the  $C^0$ -continuous field. Nevertheless, for the finest mesh M1, the two paths are completely superposed, while more and more significant deviations are observed for meshes increasingly rough, meaning that for a too rough mesh and/or too low field interpolation the smoothing by convolution of the orthogonal profile is not sufficient to guarantee regularity to the crack path. In fact, in the case of the original field the same value is attributed to the whole element area, so that the ridge is not perfectly identified. Note also that in this case smoothing is mandatory in order to find a unique maximum on orthogonal profile. A comparison between the paths obtained for the two kinds of field is observable in Fig. 19 for the roughest mesh M4. Looking at Fig. 19 it is nevertheless noteworthy that, also in worst case, the two crack paths are very close and the more regular curve is inside the convex hull of the points defining the less regular curve; thus, the proposed nodal averaging can be an effective way to bypass a non perfect local discretization. It is anyway interesting that, for the damage model presented in this section, a finer discretization is necessary when local fracture properties are needed than if only the global behaviour is requested. This depends on the fact that the history variable is far more localized than damage, since it covers about 1/3 of the damage internal length  $l_c$ .

Once the search algorithm is applied to the four meshes, it is possible to compare the corresponding crack paths. They are shown in Fig. 20, where they are superposed to the finest mesh (M1). The comparison allows to see that paths are never more distant than the size of the element of the finest mesh, with the exception of one extremity of the left crack in the centre of the specimen, obtained for mesh M4. This property shows the stability of the crack path with refinement. Again, refinement should be determined on the base of accuracy of leakage computation.

Finally, in order to illustrate the procedure in the presence of more than one damaged zone, the different steps are illustrated in Fig. 21.

## 6. Conclusion

In this contribution, an original method to track the crack path a posteriori from the results of continuum computation in the finite element frame is proposed and validated. The continuum model must be able to describe failure; for example, damage and plasticity models can be used for this purpose. A topological space is generated by a scalar field  $X(x,y)$  on a bidimensional domain, with  $X$  being the variable describing failure. The crack paths are identified as the ridges of this topological space. The method is studied for a bi-dimensional space; extension to a 3D space is straightforward

and can be done by cross-section cutting. It is also possible to identify automatically multiple cracks by resetting the field where the crack path has already been found.

The method makes use of five parameters. For all of them it is possible to provide arguments in order to fix them in a small range. The fact that the method is applied in the post-processing of non-local damage modelling does not make the simulation computationally more expensive; besides, the implementation is not intrusive in a FE code.

The procedure has been tested on the results of two mechanical simulations, obtained on different geometries and boundary conditions and with two different damage models of literature. In both cases, the algorithm has been able to find crack paths accurately, also in the presence of multiple cracks. However, in one case, the choice of the field for application of the search algorithm has not been straightforward. In fact, it has been mandatory to use a history variable field in the place of damage, since this covers a too wide zone and the ridge is not properly defined. In the other case, the model is specifically studied to represent the material near failure; hence, it has been possible to post-process directly the damage state variable.

The issue of mesh independence has been widely addressed to in the paper, both with respect to the constitutive models, which is a very well known problem in literature, and to the search algorithm. It has been shown that convergence with mesh refinement should be assessed looking at the local and not only at the global behaviour of the damage model and that this is made possible by the search algorithm which provides the crack path. In fact, eventually the model can converge globally before than locally, depending on the sensibility of the global response to the crack path direction. Mesh independence and so comparison of crack paths is improved by a field smoothing, necessary in order to obtain a regular crack path; otherwise, the crack path is bounded to follow the mesh topology and is so, in this sense, mesh dependent.

From now on, this original method coupled with the crack opening procedure [11] allows for assessing transfer properties of a concrete structure.

## Acknowledgements

Financial support was provided by the R&D department of French company EDF and by the French national "ANR Mefisto" grant. These supports are gratefully acknowledged. 3SR is part of the LabEx Tec 21 (Investissements d'Avenir - Grant agreement no. ANR-11-LABX-0030).

## References

- [1] Alfaiate J, Sluys LJ, Wells GN. On the use of embedded discontinuity elements with crack path continuity for mode I and mixed mode fracture. *Eng Fract Mech* 2002;69:661–86.
- [2] Armero F, Oller S. A general framework for continuum damage models. I. Infinitesimal plastic damage models in stress space. *Int J Solids Struct* 2000;37:7409–36.
- [3] Askes H, Sluys LJ. Remeshing strategies for adaptive ALE analysis of strain localisation. *Eur J Mech A/Solids* 2000;19(3):447–67.
- [4] *Code Aster*. Finite element software distributed by EDF. Open source and freely available. <<http://www.code-aster.org>>.
- [5] Carmeliet J, Delerue J-F, Vandersten K, Roels S. Three-dimensional liquid transport in concrete cracks. *Int J Numer Anal Methods Geomech* 2004;28:671–87.
- [6] *Cast3M*. Finite element software distributed by the CEA. Freely available for research institutes. <<http://www-cast3m.cea.fr>>.
- [7] Cazes F, Simatos A, Coret M, Combescure A. A cohesive zone model which is energetically equivalent to a gradient-enhanced coupled damage-plasticity model. *Eur J Mech A Solids* 2010;29(6):976–89.
- [8] Comi C, Mariani S, Perego U. An extended FE strategy for transition from continuum damage to mode I cohesive crack propagation. *Int J Numer Anal Methods Geomech* 2007;31(2):213–38.

- [9] Desmorat R, Gatuingt F, Ragueneau F. Nonlocal anisotropic damage model and related computational aspects for quasi-brittle materials. *Eng Fract Mech* 2007;74(10):1539–60.
- [10] Dufour F, Legrain G, Pijaudier-Cabot G, Huerta A. Estimate of crack opening from a 2d continuum-based fe computation. *Int J Numer Anal Methods Geomech* 2012;36:1813–30.
- [11] Dufour F, Pijaudier-Cabot G, Choinska M, Huerta A. Extraction of a crack opening from a continuous approach using regularized damage models. *Comput Concr* 2008;5(4):375–88.
- [12] Fremond M, Nedjar B. Damage, gradient of damage and principle of virtual power. *Int J Solids Struct* 1996;3(8):1083–103.
- [13] Geers MGD, de Borst R, Brekelmans WAM, Peerlings RHJ. Strain-based transient-gradient damage model for failure analyses. *Comput Methods Appl Mech Eng* 1998;160:133–53.
- [14] Germain P, Nguyen QS, Suquet P. Continuum thermodynamics. *J Appl Mech* 1983;50:1010–20.
- [15] Giry C, Dufour F, Mazars J. Modified nonlocal damage model based on stress state influence. *Int J Solids Struct* 2011;48(25–26):3431–43.
- [16] Granger L, Rieg CY, Touret JP, Fleury F, Nahas G, Danisch R, Brusa L, Millard A, Laborde C, Ulm F, Contri P, Schimmelpfennig K, Barr F, Firnhaber M, Gauvain J, Coulon N, Dutton LMC, Tuson A. Containment evaluation under severe accidents (CESA): synthesis of the predictive calculations and analysis of the first experimental results obtained on the Civaux mock-up. *Nucl Eng Des* 2001;209(1–3):155–63.
- [17] Greiner U, Ramm W. Air leakage characteristics in cracked concrete. *Nucl Eng Des* 1995;156(12):167–72.
- [18] Halphen B, Nguyen QS. Sur les matériaux standard généralisés. *J mécanique* 1975;14:39–73.
- [19] Hillerborg A, Modeer M, Pertersson PE. Analysis of crack formation and crack growth in concrete by means of fracture mechanics and finite elements. *Cem Concr Res* 1976;6:773–82.
- [20] La Borderie C. **Stratégies et modèles de calcul pour les structures en béton. Habilitation thesis; December 2003.**
- [21] Lemaitre J. How to use damage mechanics. *Nucl Eng Des* 1984;80:233–45.
- [22] Lemaitre J, Desmorat R. *Engineering damage mechanics: ductile, creep, fatigue and brittle failures.* Springer-Verlag; 2005.
- [23] Lorentz E, Andrieux S. A variational formulation for nonlocal damage models. *Comptes Rendus Mécanique* 1999;15:119–38.
- [24] Lorentz E, Cuvilliez S, Kazymyrenko K. Convergence of a gradient damage model toward a cohesive zone model. *Comptes Rendus Mécanique* 2011;1:20–6.
- [25] Lorentz E, Godard V. Gradient damage models: toward full-scale computations. *Comput Methods Appl Mech Eng* 2011;200(21–22):1927–44.
- [26] Matallah M, La Borderie C, Maurel O. A practical method to estimate crack openings in concrete structures. *Int J Numer Anal Methods Geomech* 2010;34(15):16151633.
- [27] Mazars Jacky. **Application de la Mécanique de l'Endommagement au Comportement non-Linéaire et à la Rupture du Béton de structures. Doctorat d'état, Université Paris 6; 1984.**
- [28] Moës N, Belytschko T. Extended finite element method for cohesive crack growth. *Eng Fract Mech* 2002;69(7):813–33.
- [29] Moes N, Dolbow J, Belytschko T. A finite element method for crack growth without remeshing. *Int J Numer Methods Eng* 1999;46:131–50.
- [30] Moes N, Gravouil A, Belytschko T. Non planar crack growth by extended finite element and level set updates. Part I: mechanical model. *Int J Numer Methods Eng* 2002;53:2549–86.
- [31] Moës N, Stolz C, Bernard P-E, Chevaugeon N. A level set based model for damage growth: the thick level set approach. *IJNME* 2010;86(3):358380.
- [32] Oliver J, Huespe AE. Continuum approach to material failure in strong discontinuity settings. *Comput Methods Appl Mech Eng* 2004;193(30–32):3195–220.
- [33] Oliver J, Huespe AE. Theoretical and computational issues in modelling material failure in strong discontinuity scenarios. *Comput Methods Appl Mech Eng* 2004;193(27–29):2987–3014.
- [34] Peerlings RHJ, de Borst R, Brekelmans WAM, de Vree JHP, Spee I. Some observations on localisation in non-local and gradient damage models. *Eur J Mech A/Solids* 1996;15(6):937–53.
- [35] Peerlings RHJ, de Borst R, Brekelmans WAM, Geers MGD. Gradient enhanced damage modelling of concrete fracture. *Int J Numer Anal Methods Geomech* 1998;3:323–42.
- [36] Pijaudier-Cabot G, Bažant Z. Nonlocal damage theory. *J Eng Mech* 1987;113:1512–33.
- [37] Pijaudier-Cabot G, Dufour F, Choinska M. Permeability due to the increase of damage in concrete: from diffuse to localised damage distributions. *J Eng Mech* 2009;135(9):1022–8.
- [38] Riva P, Brusa L, Contri P, Imperato L. Prediction of air and steam leak rate through cracked reinforced concrete panels. *Nucl Eng Des* 1999;192(1):13–30.
- [39] Rizkalla S, Lau B, Simmonds S. Air leakage characteristics in reinforced concrete. *J Struct Eng* 1984;110(5):1149–62.
- [40] Shi C, van Dam AG, van Mier JGM, Sluys LJ. **Crack interaction in concrete. In: Conference proceedings of EUROMAT99, vol. 6; 1999. p. 27–30.**
- [41] Simon H, Nahas G, Coulon N. Airsteam leakage through cracks in concrete walls. *Nucl Eng Des* 2007;237(1517):1786–94. NURETH-11 11th International Topical Meeting on Nuclear Reactor Thermal Hydraulics.
- [42] Simone A, Askes H, Peerlings RHJ, Sluys LJ. Interpolation requirements for implicit gradient-enhanced continuum damage models. *Commun Numer Methods Eng* 2003;19:563–72.